Design and evaluation of dual-resonant aggregates metaconcrete

En Zhang[a] ⓘ, Haixiang Zhao[a] ⓘ, Guoyun Lu[a*] ⓘ, Pengcheng Chen[a] ⓘ, Huiwei Yang[a] ⓘ

[a]School of Civil Engineering, Taiyuan University of Technology, Taiyuan 030024, China. E-mails: zhangen0058@link.tyut.edu.cn, zhaohaixiang0098@link.tyut.edu.cn, luguoyun@tyut.edu.cn, chenpengcheng@tyut.edu.cn, yanghuiwei@tyut.edu.cn.

* Corresponding author

https://doi.org/10.1590/1679-78257392

Abstract

Metaconcrete is a newly manmade concrete where traditional aggregates are partially replaced by resonant aggregates. The metaconcrete slab can attenuate vibration in the specific frequency bandgap which are created by the locally resonant aggregates. To enhance the attenuation performance of metaconcrete slab, a dual-resonant aggregate was designed and embedded into the metaconcrete slab. Firstly, a mass-in-(mass-in-mass) analytical model is used to predict the bandgap characteristics of dual-resonant aggregates metaconcrete. Then, eigenfrequency investigation is conducted to acquire the dispersion curve of the periodic unit cell by using finite element software COMSOL Multiphysics. The effects of the mass and stiffness ratios parameters on the characteristics of bandgap are studied. The frequency responses of the dual-resonant aggregates metaconcrete reveal that the dual-resonant aggregates metaconcrete slab can acquire vibration wave mitigation in two designed frequency bands. The results offer a base for the optimal design of the metaconcrete slab for structural protections resist vibration loading.

Keywords

Dual-resonant aggregates; Metaconcrete; Theoretical model; Bandgap characteristics; Transmission spectra

Graphical Abstract
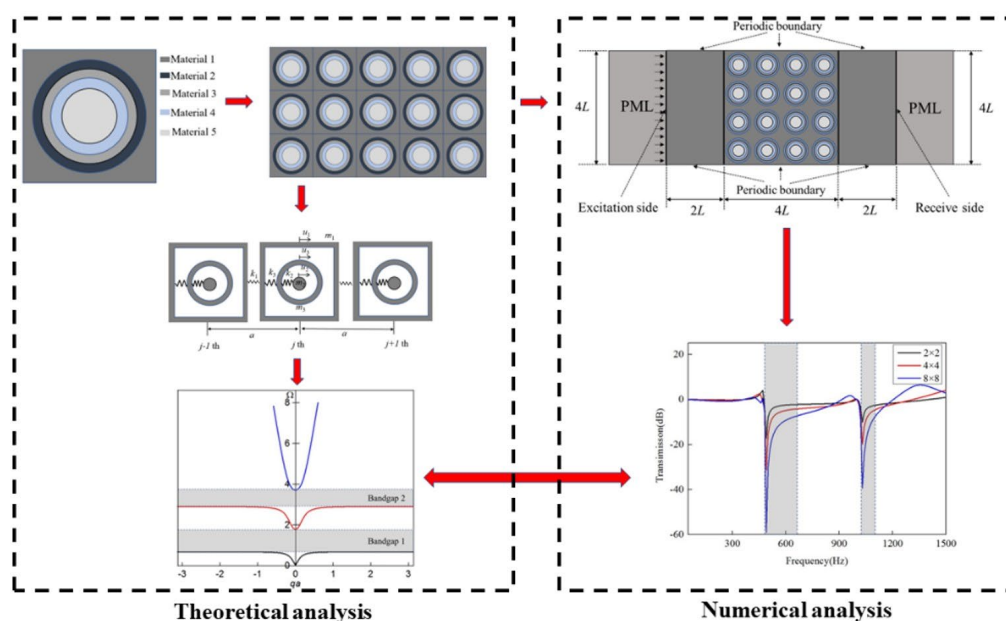
Theoretical analysis　　　　**Numerical analysis**

1 INTRODUCTION

Metamaterials are a new type of artificial material that possesses some unique properties not found in natural materials. Metamaterials have attracted increasing attention of researchers due to their promising applications in wave attenuation (Hussein et al.,2014; Liu et al.,2000; Liu et al.,2019; Mitchell et al.,2014.). Metamaterials obtain two categories: Bragg metamaterial and locally resonant metamaterial (Hussein et al.,2014.). For Bragg scattering metamaterials, it is difficult to generate bandgaps at low frequencies because it needs a very large period size and this shortcoming limits the application of Bragg metamaterial in civil engineering (Mitchell et al.,2014.). In order to further expand the application of metamaterials in low frequency condition, Liu et al. (2000) proposed a metamaterial based on locally resonance mechanism to generate bandgaps by embedding metal spheres wrapped by silicone rubber into resin matrix, which overcame the limitation of Bragg scattering metamaterials on the period size and highly enlarges the potential of metamaterials in the fields of low frequency.

Concrete structures may experience different types of natural or accidental hazardous loads in their service life, such as earthquakes, wind, accidental explosions and vehicle collision (Xu et al.,2022b.). In order to improve the load-resistance behaviors of concrete structures under dynamic load, Mitchell et al. (2014,2015,2016) proposed a new concept of concrete-like metamaterial termed as metaconcrete based on local resonance mechanism. Engineered aggregates made of heavy spherical cores wrapped by a compliant polymeric layer was inlayed into a cement matrix to form metaconcrete. Mitchell et al. (2015,2016) conducted theoretical and numerical studies to study the mitigation effectiveness of metaconcrete under blast loading, and found that particular frequency of a blast load could active resonant oscillations of heavy core within the Engineered aggregates. The resonant behavior causes the metaconcrete structure to show negative effective mass, as a result, the embedded engineered aggregates greatly enhanced the capacity of the mortar to resist blast loading. To identify the attenuation performance of metaconcrete, the transmission coefficient of metaconcrete with four different aggregates was calculated and the brittle fracture properties of the mortar and the numbers of aggregates are taken into consideration.Briccola et al. (2017) studied the attenuation properties of metaconcrete by nondestructive dynamic tests and observed a remarkable 2 order of magnitude reduction in the amplitude of the transmitted signal in metaconcrete relative to conventional concrete. Briccola et al. (2021), Briccola & Pandolfi (2021) studied the attenuation properties of metaconcrete containing two types of resonant inclusions in the sonic range and found that with respect to plain concrete, all metaconcrete specimens showed a marked (up to 80–90%) attenuation of the transmitted signal in proximity of the numerically estimated eigenfrequency of the inclusion. Kettenbeil & Ravichandran (2018) conducted plate impact experiments to study the dynamic responese of metaconcrete specimen and found that compared with a homogeneous epoxy specimen, the metaconcrete specimen led to a reduction in maximum strain of up to 72%. Gao et al. (2018) numerically studied wave attenuation performance of metaconcrete slab under two-dimensional plane wave and found that the metaconcrete slab could effectively weaken the mechanical wave and better protect the concrete mortar. Jin et al. (2020,2021) conducted analytical derivation and numerical simulation to study the dynamic respones of metaconcrete structure under explosion loading and the impact of elastic modulus and thickness of coating, aggregates kinds on the anti-explosion behavior of metaconcrete was investigated. It was found that the engineered aggregates can mitigate the damaged of metaconcrete structural against blast loading. Xu et al. (2020, 2021a) investigated the effect of design parameters on bandgaps region using numerical software COMSOL and demonstrated the efficacy of metaconcrete slab with resonant aggregates under explosion wave. Xu et al. (2021b, 2022a) conducted impulsive load experiments to investigate the influence of different kinds of aggregates and bandgaps on the stress wave mitigation of metacnocrete rod. Tan et al. (2019) developed a homogenized enriched model for analyzing the blast wave propagation in metaconcrete with viscoelastic compliant layer. Liu et al. (2021, 2022) designed single-resonator and double resonator metconcrete spcimen and studied the vibration attenuation effect of metaconcrete specimen by frequency sweeping vibration experiment. It is found that embedding double resonators into concrete is a more efficient method to improve the vibration attenuation capacity of metaconcrete, but the vibration attenuation is sensitive to the frequency and inappropriate design will aggravate the vibration. The metaconcrete mentioned above mostly focuses on single-resonant and the single negative effective mass frequency region of metaconcrete is narrow, and the further design of microstructure to improve the mitigation effect of metaconcrete is pressing needed. In order to design more bandgaps at the desired frequency region, a dual-resonant aggregates metaconcrete is needed. Besides, there are few reported studies for proposing mass-spring models to predict the frequencies of bandgaps for dual-resonant aggregates metaconcrete.

In this research, a dual-resonant aggregates metaconcrete is proposed and designed in Section 2. A mass-in-(mass-in-mass) analytical model is used to predict the bandgap characteristics of dual-resonant aggregates metaconcrete in Section 3. Then, in Section 4, eigenfrequency investigation is conducted to acquire the dispersion curve of the periodic unit cell by using finite element software COMSOL Multiphysics. The effect of the mass and stiffness ratios parameters

on the characteristics of bandgap are studied. To further describe the particular elastic waves propagation behavior in the metaconcrete, the frequency responses of the dual-resonant aggregates metaconcrete periodic structures with different number of cells are simulated in Section 5.

2 DESIGN OF THE DUAL-RESONANT AGGREGATE MEATCONCRETE

Without loss of generality, the proposed dual-resonant aggregate metaconcrete consisting of mortar matrix and dual-resonant aggregated as shown in Figure 1(a). Different from the traditional single-resonant aggregate, a dual-resonant aggregate has five parts including the host matrix and two layers (layer 1 and layer 2) inclusion as presented in Figure 1(b), and each layer composes of alternate coaxial cylindrical soft coatings and heavy cores.
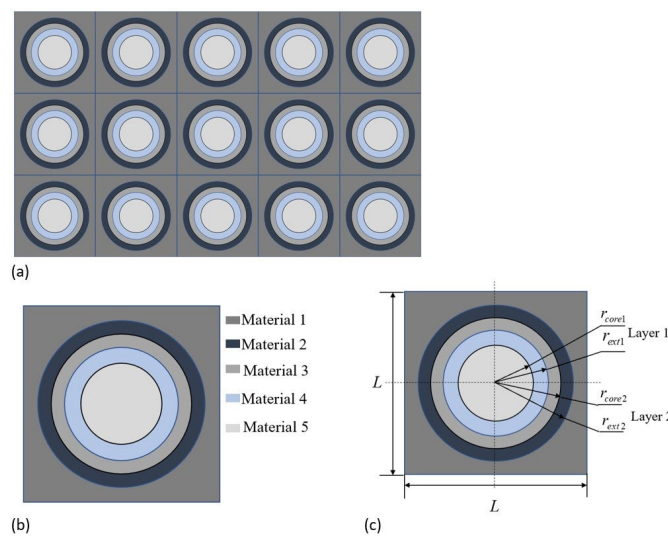

Figure 1 (a) Schematic view of the dual-resonant aggregates metaconcrete slab, (b) Single unit cell, (c) Layered structure of single unit cell.

The layered structure of single unit cell is shown in Figure 1(c). The matrix is a square shape of *L*. The external radii of the heavy core and soft coating of layer *i* (*i* = 1, 2) are bid by r_{exti} and r_{corei}, respectively. The soft coating thickness of layer *i* is bid by t_i and $t_i = r_{exti} - r_{corei}$.

3 ANALYTICAL METHOD

A mass-in-(mass-in-mass) model can be used to theoretically depict the dual-resonant aggregate unit cell as shown in Figure 2(a). In this model, the matrix is displayed by a mass of m_1, the heavy cores of layer 1 and layer 2 are represented by mass of m_2 and m_3, respectively. The soft coating of layer 1 is represented by the axial spring k_2 connecting the heavy core of layer 1 m_2 and the heavy core of layer 2 m_3. The soft coating of layer 2 is modelled by the axial spring k_3 connecting the heavy core of layer 2 m_3 and the matrix m_1.
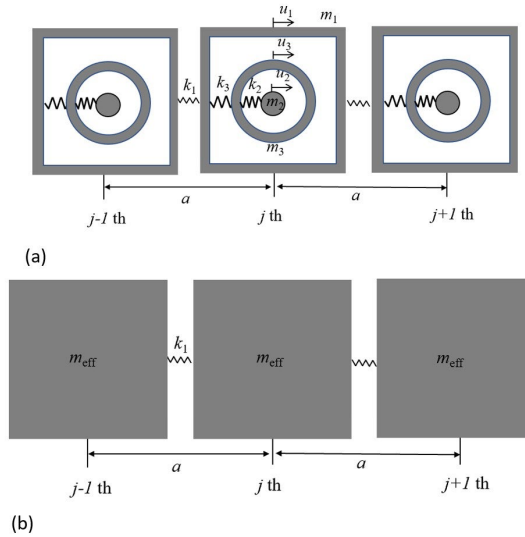
(a)

(b)

Figure 2 (a) One-dimensional lattice system, (b) Equivalent effiective model of dual-resonant aggregate metaconcrete.

The approximate values of the inner mass of the layer 1 and layer 2 can be calculated by means of Eq. (1)

$$m_i = \rho_i V_i = \rho_i \pi r_i^2 l, i = 1, 2 \tag{1}$$

Where ρ_i and V_i are the material density and volume of the i material, while the thickness and radius of the unit are presented by l and r_i, respectively.

Besides, the stiffness of equivalent spring can be calculated by means of Eq. (2) (Vo et al. 2021a,2021b):

$$
\begin{aligned}
k_1 &= \frac{A_m \mu_m}{a} \\
k_2 &= \frac{E_2 A_2}{t_1} \\
k_3 &= \frac{E_3 A_3}{t_2}
\end{aligned}
\tag{2}
$$

Where Young's modulus of the soft coating material is denoted as *E*. A_m is the nominal cross-section area of the host mortar and $A_m = l \times L$, μ_m is the lame constant of mortar and $\mu_m = \frac{E_m}{2(1 + v_m)}$. a is the lattice constant. *L* is the side length of metaconcret unit cell. Due to the shape complexity, the nominal cross-sections of the soft coating $A_i, i = 1, 2$ are obtained by FEA.

According to the dynamic equilibrium equation, the equations of motion for the j-th unit cell can be expressed by Eq. (3):

$$
\begin{aligned}
m_1^j \ddot{u}_1^j + k_1 \left(2u_1^j - u_1^{j+1} - u_1^{j-1} \right) + k_3 \left(u_1^j - u_3^j \right) &= 0 \\
m_3^j \ddot{u}_3^j + k_3 \left(u_3^j - u_1^j \right) + k_2 \left(u_3^j - u_2^j \right) &= 0 \\
m_2^j \ddot{u}_2^j + k_2 \left(u_2^j - u_3^j \right) &= 0
\end{aligned}
\tag{3}
$$

Where, $u_i^j \ (i = 1, 2, 3)$ is the displacement of the *i*-th mass in the *j*-th unit cell.

Based on the Floquent-Bloch theorem, the solution for displacement of harmonic wave of the (*j+n*)-th and *j*-th unit cell can be calculated by means of Eq. (4):

$$u^{j+n} = Ae^{i(jqa+nqa-\omega t)}$$
$$u^j = Ae^{i(jqa-\omega t)}$$

(4)

Where A is the displacement amplitude, q is the wavenumber, ω is the angular frequency, a is the length of the unit cell.

Thus

$$\ddot{u}_1^j = -\omega^2 u_1^j, \ddot{u}_2^j = -\omega^2 u_2^j, \ddot{u}_3^j = -\omega^2 u_3^j, u_1^{j+1} = u_1^j e^{iqL}, u_1^{j-1} = u_1^j e^{-iqL}$$

(5)

Thus, Eqs. (3) can be simplified as Eq. (6)

$$-m_1\omega^2 u_1^j + k_1\left(2u_1^j - u_1^j e^{iqL} - u_1^j e^{-iqL}\right) + k_3\left(u_1^j - u_3^j\right) = 0$$
$$-m_3\omega^2 u_3^j + k_3\left(u_3^j - u_1^j\right) + k_2\left(u_3^j - u_2^j\right) = 0$$
$$-m_2\omega^2 u_2^j + k_2\left(u_2^j - u_3^j\right) = 0$$

(6)

Substitute the identities Eq. (7) into Eq. (6)

$$e^{iqa} + e^{-iqa} = 2\cos(qa)$$
$$1 - \cos(qa) = 2\sin^2(qa/2)$$

(7)

The Eqs. (6) can be simplified as Eq. (8)

$$\left(-m_1\omega^2 + 2k_1 - 2k_1\cos(qa) + k_2\right)u_1^j - k_2 u_2^j = 0$$
$$-k_2 u_1^j + \left(-m_2\omega^2 + k_2 + k_3\right)u_2^j - k_3 u_3^j = 0$$
$$-k_3 u_2^j + \left(-m_3\omega^2 + k_3\right)u_3^j = 0$$

(8)

To obtain the dispersion of the lattice system, Eqs. (8) can be regarded as solving the eigenvalues of matrices and can be simplified to Eq. (9) :

$$\left[K_r - \omega^2 M_r\right]u = 0$$

(9)

Where K_r and M_r represent the stiffness matrix and the mass matrix of the system respectively, ω is the angel frequency, u is the displacement vector of the degree of freedom in the system. Thus, the Eq. (3) can be rewritten as Eq. (10):

$$\begin{bmatrix} -m_1\omega^2 + 2k_1 - 2k_1\cos(qa) + k_3 & -k_3 & 0 \\ -k_3 & -m_3\omega^2 + k_3 + k_2 & -k_2 \\ 0 & -k_2 & -m_2\omega^2 + k_2 \end{bmatrix}\begin{bmatrix} u_1^j \\ u_3^j \\ u_2^j \end{bmatrix} = 0$$

(10)

The eigenvalue problem has non-zero solution if and only if $\left[K_r - \omega^2 M_r\right] = 0$. Thus

$$\begin{bmatrix} -m_1\omega^2 + 2k_1 - 2k_1\cos(qa) + k_3 & -k_3 & 0 \\ -k_3 & -m_3\omega^2 + k_3 + k_2 & -k_2 \\ 0 & -k_2 & -m_2\omega^2 + k_2 \end{bmatrix} = 0 \tag{11}$$

Thus, the dispersion relation is given as Eq. (12):

$$\cos qa = 1 - \frac{\delta_2 \Omega^2}{2\theta_2}\left(1 + \frac{\theta_3\left(1 + \theta_1 - \Omega^2\right)}{\left[1 - \Omega^2\right]\left[1 + \delta_1 - \delta_1/\theta_1\,\Omega^2\right] - \delta_1}\right) \tag{12}$$

Where $\Omega = \omega/\omega_0$ is the non-dimensional frequency with $\omega_0 = \sqrt{k_2/m_2}$ and the mass and stiffness ratios are defined as $\theta_1 = m_2/m_3$, $\theta_2 = m_2/m_1$, $\theta_3 = m_3/m_1$, $\delta_1 = k_2/k_3$, $\delta_2 = k_2/k_1$ and $\delta_3 = k_3/k_1$.

To focus on the influence of the dual-resonant unit cell parameters on the characteristic of the bandgap frequencies, the Eq. (12) can be rewritten as Eq. (13)

$$\cos qa = 1 - \frac{\delta_2 \Omega^2}{2\theta_2}\left(1 + \frac{\theta_3\left(1 + (\theta_2/\theta_3) - \Omega^2\right)}{\left[1 - \Omega^2\right]\left[1 + \delta_2/\delta_3 - (\delta_2\theta_3/\delta_3\,\theta_2)\Omega^2\right] - \delta_2/\delta_3}\right) \tag{13}$$

According to Eq. (13), three curves of the bandgap that is the dimensionless frequency against dimensionless wave number qa, can be acquired, which presented in Figure 3(a). The parameters are selected as $\theta_2 = 8.0$, $\theta_3 = 2.0$, $\delta_2 = 0.05$ and $\delta_3 = 0.05$. It is obvious that two bandgaps(shaded area in the figure) in the low-frequency region of $\Omega = 0.68 \sim 1.78$ and $\Omega = 2.92 \sim 3.72$, in which elastic waves cannot transmit through the dual-resonant aggregates metaconcrete. Meanwhile, a passband can be observed between the two bandgaps, where no elastic wave mitigation can be discovered.

As shown in Figure 2(b), the dual-resonant aggregate metaconcrete is considered as a monatomic lattice system with the equivalent effective mass m_{eff}, which connected using spring with equivalent stiffness k_1. Thus, m_{eff} can be calculated by means of Eq. (14):

$$m_{eff}\omega^2 = 2k_1\left(1 - \cos qa\right) \tag{14}$$

The dispersion equation of the homogeneous lattice system in Figure 2(b) should consistent with the dispersion equation given in Eq. (13). So, the dimensionless effective mass m_{eff} of the lattice system can be obtained by means of Eq. (15):

$$\frac{\mathrm{m}_{eff}}{m_{st}} = \frac{\theta_2}{\theta_1 + \theta_2 + \theta_1\theta_2}\left[\frac{\theta_1}{\theta_2} + \frac{1 + \theta_1 - \Omega^2}{\left[1 - \Omega^2\right]\left[1 + \delta_1 - (\delta_1/\theta_1)\Omega^2\right] - \delta_1}\right] \tag{15}$$

Where $m_{st} = m_1 + m_2 + m_3$ represents the sum mass of the host matrix and two heavy cores.

To focus on the influence of the dual-resonant unit cell parameters on the characteristic of the bandgap frequencies, the Eq. (15) can be rewritten as Eq. (16)

$$\frac{\mathrm{m}_{eff}}{m_{st}} = \frac{1}{1 + \theta_2 + \theta_3} + \frac{\theta_3}{1 + \theta_2 + \theta_3}\left[\frac{1 + \theta_2/\theta_3 - \Omega^2}{\left[1 - \Omega^2\right]\left[1 + \delta_2/\delta_3 - (\delta_2\theta_3/\delta_3\,\theta_2)\Omega^2\right] - \delta_2/\delta_3}\right] \tag{16}$$

Figure 3(b) illustrates the figure of the dimensionless effectiveness mass m_{eff}/m_{st} against dimensionless frequency Ω. The parameters are selected as $\theta_2 = 8.0$, $\theta_3 = 2.0$, $\delta_2 = 0.05$ and $\delta_3 = 0.05$. As found in the dimensionless dispersion curve in Figure 3(a), two bandgaps (shaded area in the figure) can be found in the frequency of $\Omega = 0.68 \sim 1.78$ and $\Omega = 2.92 \sim 3.72$, which can be discovered in the dimensionless effective mass m_{eff}/m_{st} curve against dimensionless frequency Ω in Figure 3(b). By comparing Figure 3(a) and Figure 3(b), it can be concluded that frequency region of the two bandgaps can almost be calculated by the frequency region in which the effective mass m_{eff}/m_{st} is negative. The above behavior indicates that the wave energy from external excitation load must be shift and reserve into the opposite motion of the dual-resonant aggregates rather than transmitting along the metaconcrete, so the opposite mechanical motion between the dual-resonant aggregates and the host matrix impedes the incoming wave.
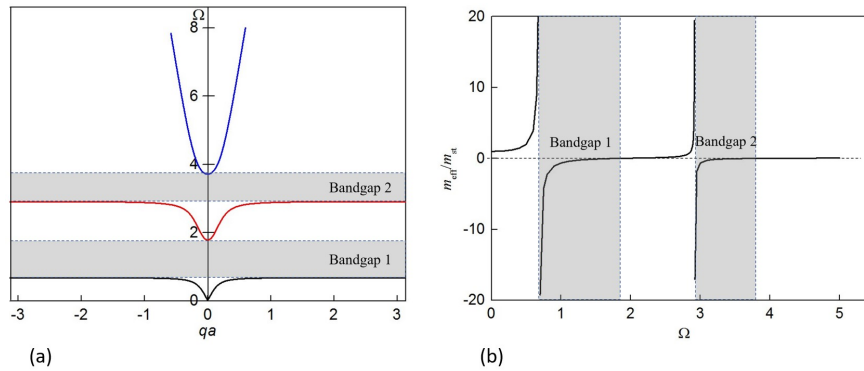

(a)   (b)

Figure 3 (a) Bandgap structure, (b) Dimensional effiective mass.

To define the location and width of the bandgaps, the dispersion in Eq. (13) can be rewritten as the starting angular frequencies and the cutoff angular frequencies, the starting angular frequencies of the bandgaps can be obtained by substituting $qa = \pi$, as Eq. (17)

$$\Omega_{i1}^2 = \frac{\delta_2/\delta_3 + \theta_2/\theta_3 + \delta_2\theta_2/\delta_3\theta_3 \pm \sqrt{\Psi - X}}{2\delta_2/\delta_3}, i = 1,2 \tag{17}$$

Where $\Psi = \left(\delta_2/\delta_3 + \theta_2/\theta_3 + \delta_2\theta_2/\delta_3\theta_3\right)^2$, $X = 4\delta_2\theta_2/\delta_3\theta_3$

The cutoff angular frequencies of the bandgaps can be obtained by substituting $qa = 0$, as Eq. (18)

$$\Omega_{i2}^2 = \frac{\delta_2/\delta_3 + \theta_2/\theta_3 + \delta_2\theta_2/\delta_3\theta_3 + \theta_2 \pm \sqrt{\Lambda - M}}{2\delta_2/\delta_3}, i = 1,2 \tag{18}$$

Where $\Lambda = \left(\delta_2/\delta_3 + \theta_2/\theta_3 + \delta_2\theta_2/\delta_3\theta_3 + \theta_2\right)^2$, $M = 4\left(1 + \theta_3 + \theta_2\right)\delta_2\theta_2/\delta_3\theta_3$

For the purpose of making clear the transfer behavior of inner masses, the relationships describing the dimensionless displacement amplitude ratios of m_2 to m_1 and m_3 to m_1 are obtained from the Eqs. (13) and (14) and are given as Eqs. (19) and (20)

$$\frac{u_2}{u_1} = \frac{1}{1 - \Omega^2\left(1 + \delta_2/\delta_3 + \left(\delta_2\theta_3/\delta_3\theta_2\right) - \left(\delta_2\theta_3/\delta_3\theta_2\right)\Omega^2\right)} \tag{19}$$

$$\frac{u_3}{u_1} = 1 + \left(\frac{\delta_2\theta_3}{\delta_3\theta_2} + \frac{1 - \Omega^2 + \theta_2/\theta_3}{\theta_2/\theta_3\left(1 + \delta_3/\delta_2\right)\left(1 - \Omega^2\right) - \left(1 - \Omega^2\right)\Omega^2 - \theta_2/\theta_3} - \frac{\delta_2}{\delta_3\theta_3}\right)\Omega^2 \tag{20}$$
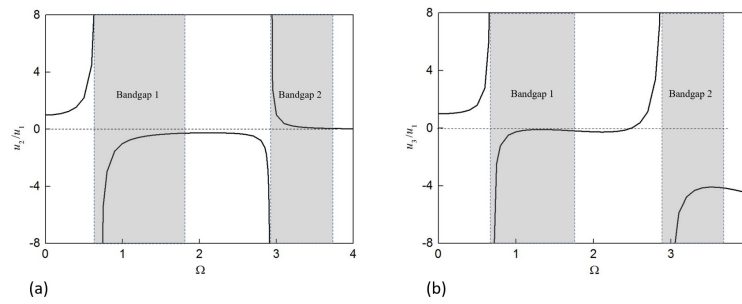
Figure 4 (a) Dimensionless displacement amplitude ratios of m2, (b) Dimensionless displacement amplitude ratios of m3.

The dimensionless displacement amplitude ratios of m_2 to m_1 and m_3 to m_1 are displayed in Figure 4. The mass ratios and stiffness ratios parameters are selected as $\theta_2 = 8.0$, $\theta_3 = 2.0$, $\delta_2 = 0.05$ and $\delta_3 = 0.05$, respectively. As shown in Figure 4, when the $\Omega \leq 0.68$, the excitation frequency is lower than the first resonant frequency, both u_2 and u_3 are in phase with u_1. However, when $0.68 \leq \Omega \leq 2.92$, the excitation frequency increases to the frequency region between the first resonant frequency and the second resonant frequency, u_2 is always out phase with u_1, while u_3 is initially out phase with u_1 then gradually becomes in phase with u_1. When $\Omega \geq 2.92$, the excitation frequency surpass the second resonant frequency, u_2 is always in phase with u_1 and u_3 is out of phase with u_1. Therefore, by comparing Figure 4 with Figure 3, it can be derived that (1) in the first bandgap, both the m_2 and m_3 prohibit the incoming wave from external excitation load by means of theirs out of phase inertial force;(2) in the second bandgap, when the excitation frequency below the resonant, m_2 works to prohibit the incoming wave by means of its own out of phase inertial force; while m_3 works to prohibit the incoming wave at the region above the second resonant frequency. These behaviors can give guidance for designing of the dual-resonant aggregate metaconcrete to obtain bandgaps in the desired frequency range.

4 NUMERICAL APPROACH

Based on the simplified one-dimensional mass-in-(mass-in-mass) model, the bandgap region has been calculated by the theoretical solution. To further study the formation of bandgap and to check the internal behavior of the aggregate in term of mode shapes. Besides, the model verification is conducted to check the accuracy of the numerical simulation in this section.

4.1 Numerical model development

In this study, commercial software COMSOL is utilized to study the bandgap properties of the dual-resonant aggregate metaconcrete. Three specimens, i.e. homogenized mortar, metaconcrete with single-resonant aggregate and metaconcrete with dual-resonant aggregate are considered as illustrated in Figure 5. The geometry of the unit cell: the matrix is a square shape with L of 100mm; for single-resonant aggregate metaconcrete unit cell, the core is a circle shape with R_c of 20mm, the coating is an annulus shape with t of 13mm, then the radius $R_a = R_c + t = 33mm$;for dual-resonant aggregate metaconcrete unit cell, the external radius of heavy core in layer 1 is $r_{core1} = 13.5mm$,the external radius of soft coating in layer 1 is $r_{ext1} = 20mm$,so the soft coating thickness of layer 1 is $t_1 = 6.5mm$;the external radius of heavy core in layer 2 is $r_{core2} = 26.5mm$,the external radius of soft coating in layer 2 is $r_{ext2} = 33mm$,so the soft coating thickness of layer 2 is $t_2 = 6.5mm$. The material properties of lead core, polyurethane coating and mortar matrix are assumed as linear elastic and the material parameters used in this numerical simulation are listed in Table 1. In addition, periodic boundary conditions are set to all sides using Floquent periodicity. Eigenfrequency investigation is conducted to acquire the dispersion curve and vibration mode shapes of the periodic metaconcrete unit cell (Oyelade et al. 2018). The relation between the eigenfrequency and the wave vector is the dispersion relation.
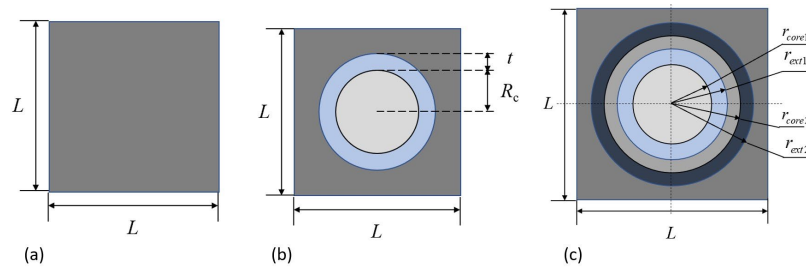
Figure 5 Model diagram of unit cell (a)Homogenized mortar, (b) Metaconcrete with single-resonant aggregate, (c) Metaconcrete with dual-resonant aggregate.

Table 1 Material parameters utilized in the numerical simulation.

Category	Material	Density (kg/m³)	Elastic modulus (GPa)	Poisson's ratio
Matrix	Mortar	2500	30	0.2
Core	Lead	11400	16	0.44
Coating layer	Polyurethane	900	0.007	0.39

4.2 Model validation

Numerical simulation method has been used to calculated the resonance frequency and bandgap frequencies in the works of Oyelade et al. (2018). To verify the numerical simulation mode in this study, the presented numerical results are compared with the results in the works of Oyelade et al. (2018) in term of the dispersion curve corresponding to eigen-frequencies of different orders. Rubber is selected as the soft coating material in the works of Oyelade et al. (2018). Figure 6 reveals the dispersion curve of single-resonant aggregate metaconcrete unit cell from numerical simulation and previous literature. As shown in Fig.6, the frequency region of bandgap of single-resonant aggregate metaconcrete is around 0.95-1.2 kHz in the works of Oyelade et al. (2018) and the frequency region of bandgap of single-resonant aggregate metaconcrete is around 0.96-1.24 kHz this study. Fig.6 shows a good agreement between the current numerical results and the previous results, which proves the accuracy of present numerical simulation model.
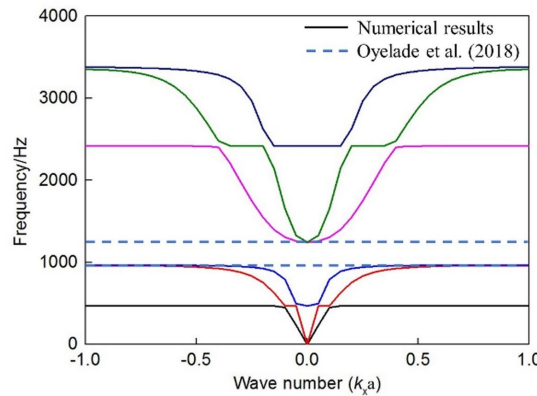

Figure 6 Comparison of the dispersion curve corresponding to eigen-frequencies of different orders between the numerical results and the previous results

4.3 Bandgap and eigen modes

Figure 7 shows the dispersive curve corresponding to eigen-frequencies of different orders of homogenized mortar, metaconcrete with single-resonant aggregate and metaconcrete with dual-resonant aggregate where the frequency is plotted against the normalized wave number. For homogenized mortar, as shown in Figure 7(a), no bandgap phenomenon is found in the frequency up to 100 kHz. For metaconcrete with single-resonant aggregate, as shown in Figure 7(b), a bandgap is observed in the band diagram, the start frequency is 407.2 Hz and the cutoff frequency is 557.7 Hz. The total width of the bandgap is 150.5 Hz. It indicates that metaconcrete with single-resonant aggregate coated by polyurethane layer can stop the propagation of elastic waves in the frequency range 407.2-557.7 Hz. For metaconcrete with dual-resonant aggregate, as shown in Figure 7(c), two bandgaps are found in the band diagram. The start frequency and cutoff frequency of the first bandgap are 485.7 Hz and 653.6 Hz, respectively. The start frequency and cutoff

frequency of the second bandgap are 1020.9 Hz and 1100.1 Hz, respectively. The total width of the bandgaps is 247.1 Hz. It indicates that metaconcrete with dual-resonant aggregate coated by polyurethane layer can stop the propagation of elastic waves in the frequency range 485.7 Hz-653.6 Hz and 1020.9 Hz -1100.1 Hz. It can be concluded that growing the layer of resonant aggregate can increase the number and the total width of bandgaps in the dispersion curve.
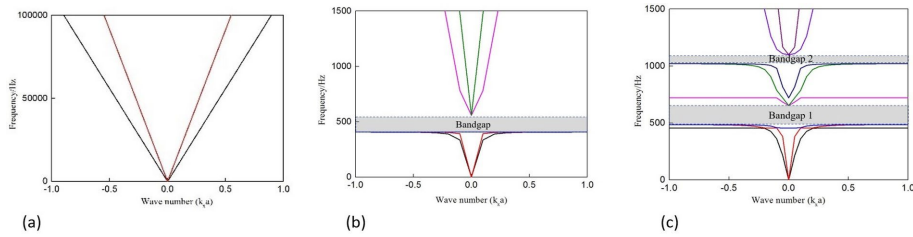

(a) (b) (c)

Figure 7 Dispersion curve corresponding to eigen-frequencies of different orders for (a) homogenized mortar, (b) metaconcrete with single-resonantaggregate, (c) metaconcrete with dual-resonant aggregate.

In order to further explore the vibration characteristics of the dual-resonant aggregate at the start frequency and cutoff frequency of the first bandgap and the second bandgap, the vibration mode shape of metaconcrete unit cell embedded with dual-resonant aggregate is shown in Figure 8. The arrows and colors refer to the displacement of the unit cell.
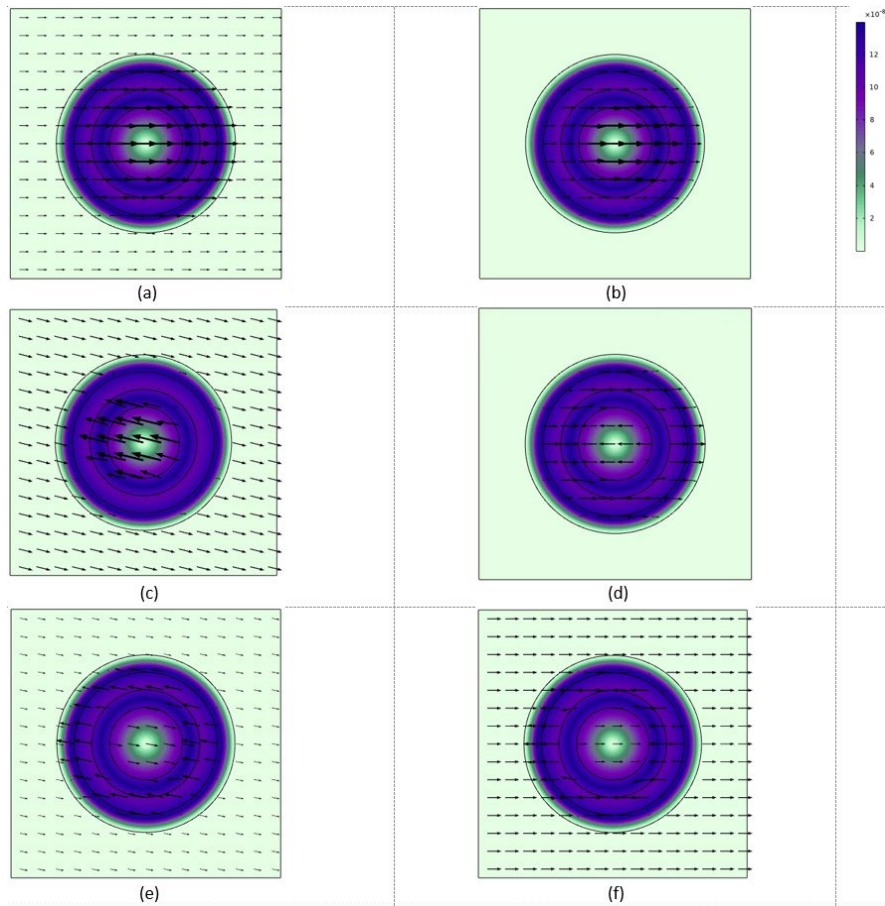

Figure 8 Displacement fields of dual-resonant aggregate metaconcete under different frequency region (a) 382.1 Hz, (b) 486.7 Hz, (c)653.6 Hz, (d) 1020.9 Hz, (e) 1100.1 Hz, (f) 1167 Hz.

For dual-resonant aggregates metaconcrete, the displacement fields are shown in Figure 8. When the frequency is lower than the first resonant frequency, the metaconcrete unit cell move as a whole, so the cores in layer 1 and layer 2 and the matrix move in the identical direction, as shown in Figure 8(a). The displacement of the cores in layer 1 and layer 2 are much larger than that of the matrix. The vibration characteristic is basically consistent with the theoretical analysis in section 3 above. At the start frequency of the first bandgap, as shown in Figure 8(b), the dual-resonant aggregate moves as a whole while the matrix keeps in a fixed position. Besides,

as shown in Figure 8(b), the ratio between the displacement of dual-resonant aggregate and the matrix is very large which is consistent with the theoretical analysis in section 3 above where the absolute value of the ratio curve is very large near the first resonant frequency. At the cutoff frequency of the first bandgap, as shown in Figure 8(c), the cores in layer 1 and the matrix move to opposite direction. The cores in layer 2 and the matrix move to same direction. At the start frequency of the second bandgap, as shown in Figure 8(d), the cores in layer 1 and the cores in layer 2 move to opposite direction, while the matrix keeps in a fixed position. Besides, as shown in Figure 8(d), the ratio between the displacement of dual-resonant aggregate and the matrix is very large which is consistent with the theoretical analysis in section 3 above where the absolute value of the ratio curve is very large near the second resonant frequency. As shown in Figure 8(e), at the cutoff frequency of the second bandgap, the cores in layer 1 and the matrix move to same direction and the cores in layer 2 and the matrix move to opposite direction. At the frequency exceeding the cutoff frequency of the second bandgap, as shown in Figure 8(f), the cores in layer 1 and the matrix move to same direction and the cores in layer 2 and the matrix move to opposite direction, the displacement of the matrix is much larger than that of the cores in layer 1 and layer 2. The vibration characteristics of the dual-resonant aggregate metaconcrete unit cell calculated by COMSOL are mostly consistent with the results of the theoretical analysis in section 3. The reason for the slight difference between the numerical results and theoretical analysis results is that in numerical study, the coatings, the cores and the matrix can act as lumped mass, while in theoretical analysis, only the cores and the matrix are simplified as lumped mass, the coating is simplified as massless spring.

4.4 Parametric investigations

In this section, parametric study is conducted to study the effect of various critical parameters on the bandgap characteristics of dual-resonant metaconcrete unit cell in eigenfrequency. According to the analytical results in section 3, the stiffness ratios parameters and mass ratios parameters have a great influence on bandgap frequency region. In this section, the method of changing the elastic modulus of the coatings and the density of the cores in the dual-resonant aggregate is used to change the parameters of mass ratio and stiffness ratio, while keeping the material parameters of the matrix unchanged. In addition, the geometry of the entire dual-resonant aggregate metaconcrete unit cell remains unchanged. The results of the analyses are presented in terms of the start frequency and the cutoff frequency of the first bandgap and the second bandgap of the dual-resonant metaconcrete unit cell. This section is conducted to gain further insight of the performance of the metaconcrete unit cell. The elastic modulus of the coatings in layer 1 and layer 2 are denoted as E_{ext1} and E_{ext2}, respectively. The densities of the cores in layer 1 and layer 2 are denoted as ρ_{core1} and ρ_{core2}, respectively.

4.4.1 Influence of coating modulus in layer 1

To study the effect of coating modulus in layer 1 on the bandgap, six elastic moduli are considered in the numerical numerical simulation. As shown in Table 2, the geometric dimensions of the dual-resonant aggregate metaconcrete unit cell remain unchanged in this section. E_{ext2}, ρ_{core1} and ρ_{core2} remain the same, while E_{ext1} changes as $E_{ext1} = \alpha E_{ext2}, \alpha = 0.2, 0.5, 1.0, 1.5, 2.0, 2.5$.

Table 2 Relative elastic ratio α utilized in the numerical simulation.

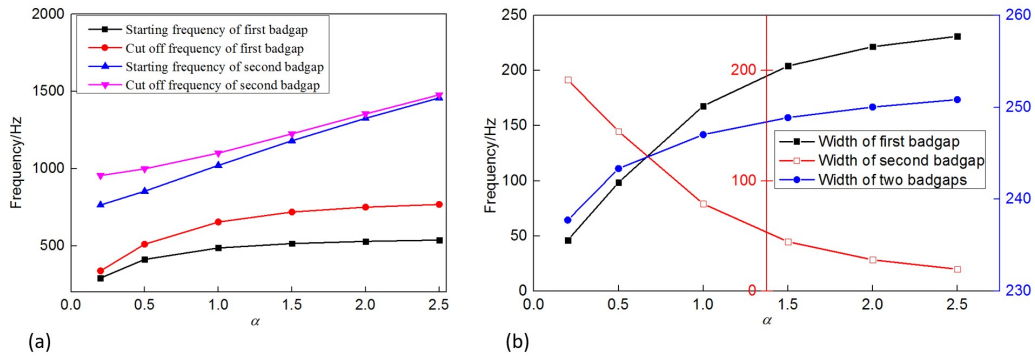| Geometric dimensions	ρ_{core1} (kg/m³)	ρ_{core2} (kg/m³)	E_{ext1} (GPa)	E_{ext2} (GPa)	Relative elastic ratio α
$r_{core1} = 13.5mm$	11400	11400	0.0014	0.007	0.2
$r_{ext1} = 20mm$			0.0035		0.5
$r_{core2} = 26.5mm$			0.007		1.0
$r_{ext2} = 33mm$			0.0105		1.5
			0.014		2.0
			0.0175		2.5

Figure 9 (a) frequency region vs. α , (b) width of the bandgaps vs. α .

Figure 9(a) presents the calculated results of the start frequency and cutoff frequency of the first bandgap and the second bandgap with reference to the elastic modulus of coating α in layer 1. It can be seen that when α increases, the starting frequency and cutoff frequency of the first bandgap of the dual-resonant aggregates metaconcrete become larger. For instance, the frequency range increases from 290.6 Hz- 336.8 Hz to 536.5 Hz-767.5Hz with the elastic modulus of coating α changing from 0.2 to 2.5. Meanwhile, the increasing speed of the starting frequency is smaller than that of the cutoff frequency, as a result, the width of the first bandgap becomes larger, as shown in Figure 9(b). For the second bandgap, when α increases, the starting frequency and cutoff frequency becomes larger but the increasing speed of the starting frequency is larger than that of the cutoff frequency. For instance, the frequency range increases from763.4 Hz- 954.9 Hz to 1458.1 Hz-1477.8 Hz with the elastic modulus of coating α changing from 0.2 to 2.5. As a result, the width of the second bandgap becomes small, as shown in Figure 9(b). The overall width of the first bandgap and the second bandgap becomes larger with the increase of the α , as shown in Figure 9(b). To enlarge the overall width, it is suggested to selecte a larger α .

4.4.2 Influence of coating modulus in layer 2

In this section, to study the effect of coating modulus in layer 2 on the bandgap, six elastic moduli are considered in the numerical simulation. As shown in Table 3, the geometric dimensions of the dual-resonant aggregate metaconcrete unit cell remain unchanged in this section. E_{ext1} , ρ_{core1} and ρ_{core2} remain the same, while E_{ext2} changes as $E_{ext2} = \beta E_{ext1}, \beta = 0.2, 0.5, 1.0, 1.5, 2.0, 2.5$.

Table 3 Relative elastic ratio β utilized in the numerical simulation.

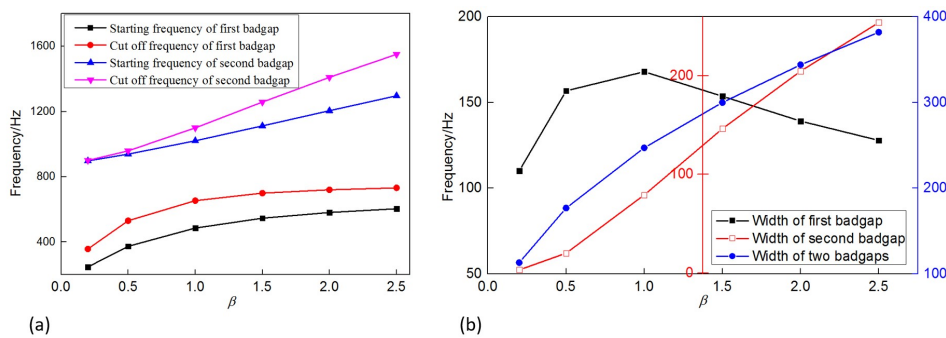| Geometric dimensions	ρ_{core1} (kg/m³)	ρ_{core2} (kg/m³)	E_{ext1} (GPa)	E_{ext2} (GPa)	Relative elastic ratio β
$r_{core1} = 13.5mm$	11400	11400	0.007	0.0014	0.2
$r_{ext1} = 20mm$				0.0035	0.5
$r_{core2} = 26.5mm$				0.007	1.0
				0.0105	1.5
$r_{ext2} = 33mm$				0.014	2.0
				0.0175	2.5

Figure 10 (a) frequency region vs. β , (b) width of the bandgaps vs. β .

Figure 10(a) presents the calculated results of the start frequency and cutoff frequency of the first bandgap and the second bandgap with reference to the elastic modulus of coating β in layer 2. It can be seen that when β increases, the starting frequency and cutoff frequency of the first bandgap of the dual-resonant aggregates metaconcrete become larger. As shown in Figure 10(b), for the width of the first bandgap, when β is less than 1, the width tends to increase, and when β is greater than 1, it becomes a decreasing trend. Besides, when β increases, the starting frequency and cutoff frequency of the second bandgap of the dual-resonant aggregates metaconcrete become larger, as shown in Figure 10(a). The increasing speed of the starting frequency is smaller than that of the cutoff frequency. For instance, the frequency range increases from 897.3 Hz- 900.4 Hz to 1296.7 Hz-1500.8 Hz with the elastic modulus of coating β changing from 0.2 to 2.5. As a result, for the width the second bandgap, it becomes larger as the β increase, as shown in Figure 10(b). Consequently, the overall width of the first bandgap and the second bandgap becomes larger with the increase of the β, as shown in Figure 10(b). To enlarge the overall width, it is suggested to selecte a larger β.

4.4.3 Influence of heavy core density in layer 1

In this section, to investigate the influence of heavy core density in layer 1 on the bandgap, six heavy core densities are considered in the numerical simulation. As shown in Table 4, the geometric dimensions of the dual-resonant aggregate metaconcrete unit cell remain unchanged in this section. E_{ext1}, E_{ext2} and ρ_{core2} remain the same, while ρ_{core1} changes as $\rho_{core1} = \gamma \rho_{core2}$ and $\gamma = 0.25, 0.5, 1.0, 1.5, 2.0, 2.5$.

Table 4 Relative density ratio γ utilized in the numerical simulation.

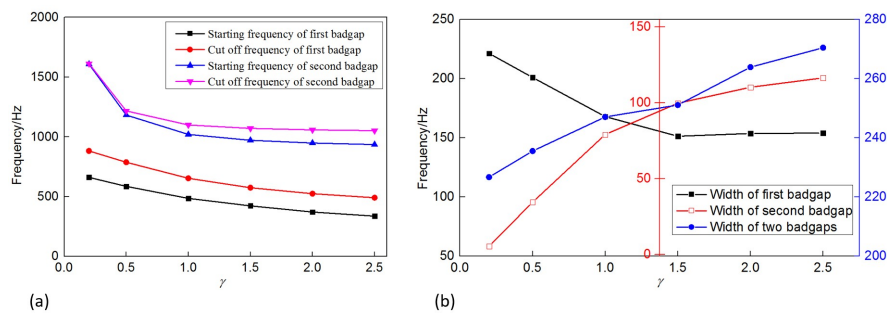| Geometric dimensions	ρ_{core1} (kg/m³)	ρ_{core2} (kg/m³)	E_{ext1} (GPa)	E_{ext2} (GPa)	Relative density ratio γ
$r_{core1} = 13.5mm$	2850	11400	0.007	0.007	0.25
$r_{ext1} = 20mm$	5700				0.5
$r_{core2} = 26.5mm$	11400				1.0
	17100				1.5
$r_{ext2} = 33mm$	22800				2.0
	28500				2.5

Figure 11 (a) frequency region vs. γ , (b) width of the bandgaps vs. γ .

Figure 11(a) presents the calculated results of the start frequency and cutoff frequency of the first bandgap and the second bandgap with reference to the heavy core density γ in layer 1. It can be seen that when γ increases, the starting frequency and cutoff frequency of the first bandgap of the dual-resonant aggregates metaconcrete become small. For instance, the frequency range decreases from 661.2 Hz- 882.5 Hz to 337.3 Hz-491.2 Hz with the heavy core density γ changing from 0.2 to 2.5.As shown in Figure 11(b), for the width of the first bandgap, when γ is less than 1.5, the width tends to decrease, and when γ is greater than 1.5, it becomes a constant trend. For the second bandgap, when γ increases, the starting frequency and cutoff frequency become small but the decreasing speed of the starting frequency is smaller than that of the cutoff frequency. For instance, the frequency range decreases from1607.7 Hz- 1613.2 Hz to 935.9 Hz-1052.4 Hz with the heavy core density γ changing from 0.2 to 2.5. Consequently, the overall width of the first bandgap and the second bandgap become larger with the increase of γ , as shown in Figure 11(b). To enlarge the overall width, it is suggested to selecte a larger γ .

4.4.4 Influence of heavy core density in layer 2

In this section, to examine the influence of heavy core density in layer 2 on the bandgap, six heavy core densities are considered in the numerical simulation. As shown in Table 5, the geometric dimensions of the dual-resonant aggregate metaconcrete unit cell remain unchanged in this section. E_{ext1}, E_{ext2} and ρ_{core1} remain the same, while ρ_{core2} changes as $\rho_{core2} = \eta\rho_{core1}$ and $\eta = 0.25, 0.5, 1.0, 1.5, 2.0, 2.5$.

Figure 12(a) presents the calculated results of the start frequency and cutoff frequency of the first bandgap and the second bandgap with reference to the heavy core density η in layer 2. It can be seen that when η increases, the starting frequency of the first bandgap of the dual-resonant aggregates metaconcrete remains unchanged and the cutoff frequency of the first bandgap of the dual-resonant aggregates metaconcrete becomes small. For instance, the frequency ranges from 539.1 Hz- 656.5 Hz to 394.5 Hz-647.9 Hz with the heavy core density γ changing from 0.2 to 2.5. As a result, the width of the first bandgap becomes wider with the rising heavy core density η in layer 2, as shown in Figure 12(b). For the second bandgap, when η increases, the starting frequency and cutoff frequency become small. For instance, the frequency range decreases from 1857.6 Hz- 1925.1 Hz to 807.7 Hz-860.7 Hz with the heavy core density η changing from 0.2 to 2.5. As shown in Figure 12(b), for the width of the second bandgap, when η is less than 1, the width tends to increase, and when η is greater than 1, it becomes a decreasing trend. Consequently, the overall width of the first bandgap and the second bandgap becomes larger with the increase of η , as shown in Figure 12(b). To enlarge the overall width, it is recommended to choose a large η .

Table 5 Relative density ratio η utilized in the numerical simulation.

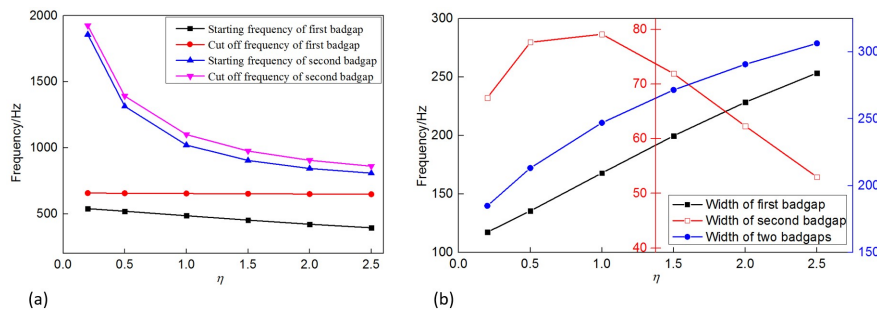| Geometric dimensions	ρ_{core1} (kg/m³)	ρ_{core2} (kg/m³)	E_{ext1} (GPa)	E_{ext2} (GPa)	Relative density ratio η
$r_{core1} = 13.5mm$	11400	2850	0.007	0.007	0.25
$r_{ext1} = 20mm$		5700			0.5
$r_{core2} = 26.5mm$		11400			1.0
		17100			1.5
$r_{ext2} = 33mm$		22800			2.0
		28500			2.5

Figure 12 (a) frequency region vs. η ,(b) width of the bandgaps vs. η .

5 WAVE TRANSMISSION SPECTRA OF METACONCRETE SLAB

Although the ideal locally resonant metaconcrete has a perfect elastic wave shielding effect in its band gap range, it is based on the result of an infinite periodic structure. Even if the smaller attenuation effect can be continuously accumulated to achieve the purpose of eliminating elastic waves. In practical applications, only finite periodic structures can be used, which makes some elastic waves in the band gap frequency range of the band gap structure unable to attenuate to a certain extent and still pass through the finite structure. Therefore, for the finite periodic locally resonant metaconcrete, the band gap structure as the only reference may not be convincing enough, and it needs to be supported by indicators and data that can reflect the elastic wave transmission characteristics in the finite structure. To study the mitigation effect of the finite dual-resonant aggregates metaconcrete structure, the transmission spectra of the

corresponding period metaconcrete slab with different number of unit cell are computed by the frequency response analysis in COMSOL. The schematic diagram of the dual-resonant aggregates metaconcrete slab model is shown in Figure 13. The structural form and geometric size of the resonators are consistent with section 4.1. The interfaces between the core and the coating and the interfaces between the aggregates and the matrix are assumed to be in perfect contact with the simulation. In addition, period boundary conditions (PBC) are applied along top sideline and bottom sideline of the metaconcrete slab, and the type of periodicity is set as continuous (Xu et al. 2020). To avoid reflection, two perfect matched layers (PMLs) are applied in the x direction. A dynamic displacement with a frequency ranging from 50 Hz to 1500 Hz in the horizontal direction of sinusoidal vibration. The periodic metaconcrete slab consists of 2×2, 4×4 and 8×8 resonant aggregates, respectively. In order to compare the vibration wave mitigation ability of single-resonant metaconcret slab and dual-resonant metaconcret slab, single-resonant metaconcret slab with the same structural form and geometric size is also established.

To evaluate the vibration mitigation effect of metaconcrete, the transmission can be calculated by means of Eq. (21)

$$Transmission = 20\lg\left(A_o / A_i\right) \tag{21}$$

Where A_i and A_o is the average value of the prescribed displacement on the input side and output side of the metaconcrete slab in the x direction, respectively. Transmission represents the mitigation of the vibration energy.
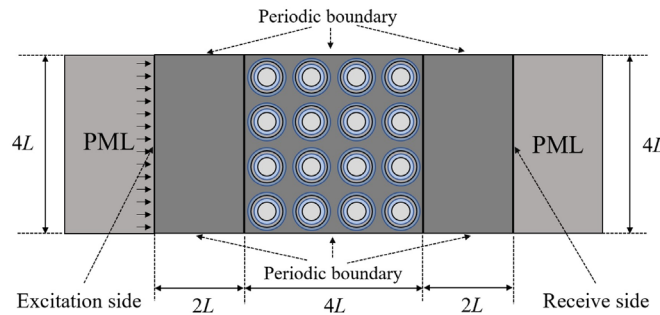

Figure 13 Model diagram of the metaconcrete slab with dual-resonant aggregates.

(a)   (b)
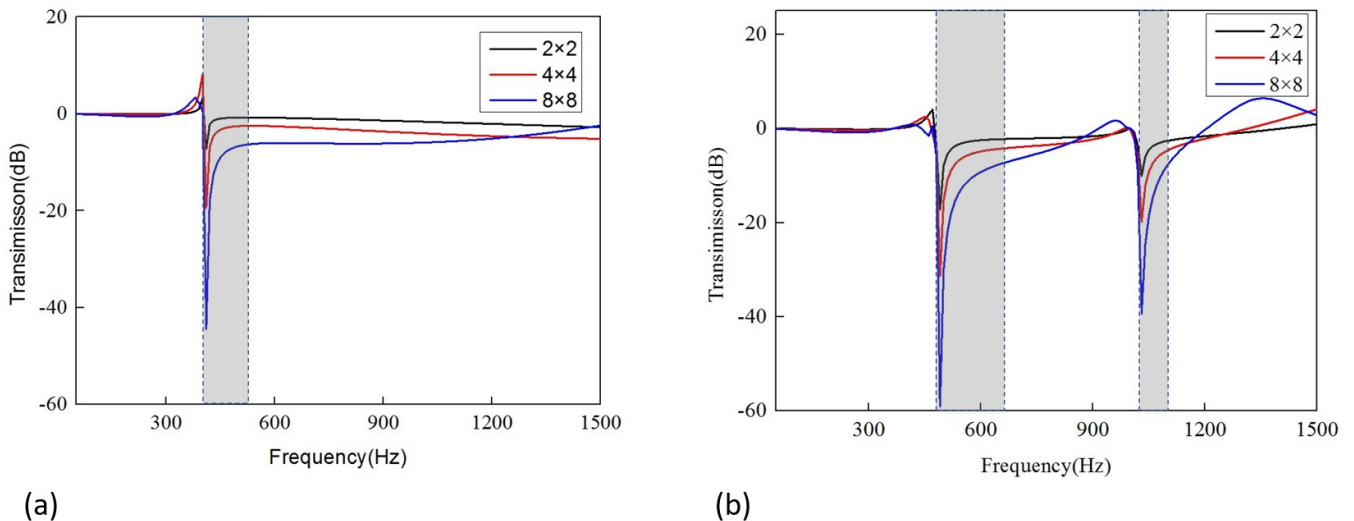
Figure 14 Transmission spectra of the (a) single-resonant aggregates, (b) dual-resonant aggregates metaconcrete slab.

Figure 14 presents the transmission spectra of the single-resonant aggregates and dual-resonant aggregates metaconcrete slab with different number resonators. The frame frequency areas in Figure 14(a) and Figure 14 (b) are consistent with the bandgap frequency region in Figure 7(a) and Figure 7(b). In the bandgap frequencies region, significant wave attenuation was observed. For metaconcrete, there are sharp dips at the staring frequency of bandgap, this is consistent with the results in the works of Liu et al. (2021,2022). For single-resonator aggregate metaconcrete, vibration can be attenuated in the one bandgap described as frame area. For dual-resonators aggregate metaconcrete, vibration can be attenuated in the two bandgaps. It is found that by embedding dual-resonators aggregates into

metaconcret, the bandgaps can be extended to two ranges because of the presence of more localized resonance modes. Besides, it is found that increasing the number of the unit cells is another effective method to enhance the mitigation effects of metaconcrete slab. For single-resonant aggregate metaconcrete slab, as shown in Figure 14(a), the largest mitigation of the vibration is about 7.28 dB for 2×2 model. The largest mitigation can be enhanced to about 19.39 dB for the model containing 4×4 resonant aggregates. When the number of unit cells increases to 8×8, the largest mitigation can be enhanced to about 44.41dB. For dual-resonant aggregate metaconcrete slab, as shown in Figure 14(b), the largest mitigation of metaconcrete slab is located in the starting frequency of the second bandgap. For the metaconcrete containing 2×2, 4×4 and 8×8 resonant aggregates, the largest mitigation is about 17.22 dB, 31.24 dB and 59.05 dB for the first bandgap and 10.04 dB, 19.86 dB and 39.32 dB for the second bandgap. Consequently, the metaconcrete slab containing single-resonant and dual-resonant aggregates can attenuate the vibration effectively. The mitigation effects can be improved through aggregates design as well as the increase of the unit cells in metaconcrete slab.

6 CONCLUSION

In this study, a dual-resonant aggregates metaconcrete slab is proposed and the vibration attenuation performance of the proposed metaconcrete slab were theoretically and numerically investigated. A mass-in-(mass-in-mass) model is used to depict the vibration characteristic of the dual-resonant aggregates. The theoretical results prove that two bandgaps appear in the dimensional dispersion curve as a result of more localized vibration modes present in the dual-resonant aggregates. The numerically calculated bandgaps and vibration mode characteristics agree well with the analytical prediction. The location and width of the bandgaps for dual-resonant aggregates are sensitive to the mass ratio and stiffness ratio parameters. Increasing the mass ratio parameters and stiffness ratio parameters could accomplish a wider bandgaps region. The dual-resonant aggregates configuration could be tuned to mitigate vibration load at the target frequency range. The metaconcrete slab consisting of resonant aggregates are certified to attenuate vibration in the designed bandgaps by casting the frequency response analysis. The results obtained in this study demonstrate that vibration attenuation effects of resonant aggregates metaconcrete slab can be improved by increasing the numbers of coating layers in resonant aggregate and the numbers of resonant aggregates. In general, the results from this study demonstrate that the dual-resonator metaconcrete works better than the conventional single-resonator metaconcrete for mechanical wave attenuation. It has a great potential in protective structures. However, further researches need to be conducted to investigate the attenuation effect of combined use of various dual-resonator aggregates and also to execute frequency-sweeping vibration experiment and/or impact experiment to experimentally verify the performances of the dual-resonator metaconcrete.

Acknowledgements

Author's Contribuitions: Conceptualization, En Zhang and Guoyun Lu; Methodology, En Zhang; Investigation, En Zhang, Haixiang Zhao, Guoyun Lu, Pengcheng Chen and Huiwei Yang; Writing - original draft, En Zhang and Haixiang Zhao; Writing - review & editing, En Zhang, Haixiang Zhao Guoyun Lu, Pengcheng Chen and Huiwei Yang; Funding acquisition, Guoyun Lu and Pengcheng Chen; Resources, Guoyun Lu; Supervision, Guoyun Lu.

Editor: Marco L. Bittencourt

References

Briccola, D., Cuni, M., De Juli, A., Ortiz, M., Pandolfi, A. (2021). Experimental Validation of the Attenuation Properties in the Sonic Range of Metaconcrete Containing Two Types of Resonant Inclusions. Experimental Mechanics 61:515–32.

Briccola, D., Ortiz, M., Pandolfi, A. (2017). Experimental Validation of Metaconcrete Blast Mitigation Properties. Journal of Applied Mechanics 84:031001.

Briccola, D., Pandolfi, A. (2021). Analysis on the Dynamic Wave Attenuation Properties of Metaconcrete Considering a Quasi-Random Arrangement of Inclusions. Frontiers in Materials 7:615189.

Gao, Y.J., Fan, H.L., Zhang, B., Jin, F.N. (2018). Wave attenuation of super-material wave absorbing concrete panel subjected to two-dimensional plane wave. Journal of Vibration and Shock 37: 39–44 (in Chinese).

Hussein, M.I., Leamy, M.J., Ruzzene, M. (2014). Dynamics of Phononic Materials and Structures: Historical Origins, Recent Progress, and Future Outlook. Applied Mechanics Reviews 66:040802.

Jin, H.X., Hao, H., Chen, W.S., Xu, C. (2021). Spall Behaviors of Metaconcrete: 3D Meso-Scale Modelling. International Journal of Structural Stability and Dynamics 21:2150121.

Jin, H.X., Hao, H., Hao, Y.F., Chen, W.S. (2020). Predicting the response of locally resonant concrete structure under blast load. Construction and Building Materials 252:118920.

Kettenbeil, C., Ravichandran, G. (2018). Experimental investigation of the dynamic behavior of metaconcrete. International Journal of Impact Engineering 111:199–207.

Liu, Y., An, X.Y., Chen, H.L., Fan, H.L. (2021). Vibration attenuation of finite-size metaconcrete: Mechanism, prediction and verification. Composites Part A 143: 106294.

Liu, Y., Shi, D.Y., He, H.G., Liu, S.F., Fan, H.L. (2022). Double-resonator based metaconcrete composite slabs and vibration attenuation mechanism. Engineering Structures 262:114392.

Liu, Z.B., Rumpler, R., Feng, L.P. (2019). Investigation of the sound transmission through a locally resonant metamaterial cylindrical shell in the ring frequency region. Journal of Applied Physics 125: 115105.

Liu, Z.Y., Zhang, X.X., Mao, Y.W., Zhu, Y.Y., Yang, Z.Y., Chan, C.T., Sheng, P. (2000). Locally resonant sonic materials. Science 289:1734–6.

Mitchell, S.J., Pandolfi, A., Ortiz, M. (2014). Metaconcrete: designed aggregates to enhance dynamic performance. Journal of the Mechanics and Physics of Solids 65:69–81.

Mitchell, S.J., Pandolfi, A., Ortiz, M. (2015). Investigation of elastic wave transmission in a metaconcrete slab. Mechanics of Materials 91:295–303.

Mitchell, S.J., Pandolfi, A., Ortiz, M. (2016). Effect of brittle fracture in a metaconcrete slab under shock loading. Journal of Engineering Mechanics 142: 04016010.

Oyelade, A.O., Abiodun, Y.O., Sadiq, M.O. (2018). Dynamic behaviour of concrete containing aggregate resonant frequency. Journal of Computational Applied Mechanics 49:380-385.

Tan, S.H., Poh, L.H., Tkalich, D. (2019). Homogenized enriched model for blast wave propagation in metaconcrete with viscoelastic compliant layer. International Journal for Numerical Methods in Engineering 119:1395–418.

Vo, N.H., Pham, T.M., Bi, K.M., Chen, W.S., Hao, H. (2021a). Stress Wave Mitigation Properties of Dual-meta Panels against Blast Loads. International Journal of Impact Engineering 154:103877.

Vo, N.H., Pham, T.M., Bi, K.M., Hao, H. (2021b). Model for analytical investigation on meta-lattice truss for low-frequency spatial wave manipulation. Wave Motion 103:102735.

Xu, C., Chen, W.S., Hao, H. (2020). The influence of design parameters of engineered aggregate in metaconcrete on bandgap region. Journal of the Mechanics and Physics of Solids 139:103929.

Xu, C., Chen, W.S., Hao, H., Bi, K.M., Pham, T.M. (2022a). Experimental and numerical assessment of stress wave attenuation of metaconcrete rods subjected to impulsive loads. International Journal of Impact Engineering 159:104052.

Xu, C., Chen, W.S., Hao, H., Jin, H.X. (2021a). Effect of engineered aggregate configuration and design on stress wave attenuation of metaconcrete rod structure. International Journal of Solids and Structures 232:111182.

Xu, C., Chen, W.S., Hao, H., Pham, T.M., Bi, K.M. (2021b). Damping properties and dynamic responses of metaconcrete beam structures subjected to transverse loading. Construction and Building Materials 311: 125273.

Xu, C., Chen, W.S., Hao, H., Pham, T.M., Li, Z.X., Jin, H.X. (2022b). Dynamic compressive properties of metaconcrete material. Construction and Building Materials 351:128974.